Performance Characterization of Phase Gradient Autofocus for Inverse Synthetic Aperture LADAR

Casey J. Pellizzari
Air Force Research Laboratory
535 Lipoa Parkway, Suite 200
Kihei, HI 96753

Mark F. Spencer
Air Force Institute of Technology
2950 Hobson Way
Dayton, OH 45433

Brandoch Calef
Boeing, LTS.
535 Lipoa Parkway, Suite 200
Kihei, HI 96753

Jeremy Bos
Air Force Research Laboratory
535 Lipoa Parkway, Suite 200
Kihei, HI 96753

Skip Williams
Air Force Research Laboratory
535 Lipoa Parkway, Suite 200
Kihei, HI 96753

Daniel C. Senft
Air Force Research Laboratory
3550 Aberdeen Ave SE
Kirtland AFB, NM 87117

Stacie E. Williams
Air Force Research Laboratory
535 Lipoa Parkway, Suite 200
Kihei, HI 96753

Abstract—Phase Gradient Autofocus (PGA) is an effective algorithm for estimating and removing piston-phase errors from spotlight-mode synthetic aperture radar (SAR) data. For target scenes dominated by a point source, the algorithm has been shown to be optimal in the sense that it approaches the Cramér-Rao bound for carrier-to-noise ratios (CNRs) as low as -5 dB. In this paper, we explore PGA's effectiveness against ground-based inverse synthetic aperture LADAR (ISAL) observations of spacecraft, where the target characteristics and phase errors are quite different than in the SAR case. At optical wavelengths, the power spectrum of the piston-phase errors will be dominated less by platform motion and more by atmospheric variations. In addition, space objects will have fewer range-resolution cells across them than would a typical extended SAR scene. This research characterizes the performance limitations of PGA for an ISAL system as a function of CNR and the number of range-resolution cells across the scene. A high-fidelity wave-optics simulation is used to generate representative test data for input to the PGA algorithm. Emphasis is placed on finding the lower limits of performance for which image reconstruction is possible.

TABLE OF CONTENTS

1. INTRODUCTION

Spotlight-mode Synthetic Aperture Radar (SAR) systems use radio-frequency (RF) illumination and relative movement between the object and observer to synthesize large apertures and produce high-resolution terrain images [1]. As such, SAR system concepts may be applied to laser radar (LADAR) systems; specifically, inverse synthetic aperture LADAR (ISAL) systems for the purpose of imaging geosynchronous Earth orbit (GEO) space objects [2, 3]. The benefit of ISAL systems is that they only require meter-class telescopes to obtain high-resolution images of GEO space objects. This is in stark contrast to conventional imaging systems, which require 10 m apertures or more because of the large distances involved (around 40 Mm).

Just as large-aperture telescopes have their drawbacks, so do ISAL systems. One must trade the difficulties associated with building and operating a 10 m class telescope for the difficulties associated with actively illuminating a distant object and coherently detecting the return signal. Therefore, it is important to fully understand and characterize the performance limitations of ISAL systems prior to their construction.

One performance limitation of an ISAL system is piston-phase error, and there are many factors which contribute to this performance limitation. These factors include residual platform motion, local oscillator instabilities, sensor noise, speckle decorrelation, and atmospheric turbulence. With that said, phase gradient autofocus (PGA) is an effective algorithm for estimating and removing these piston-phase errors from ISAL images; however, there are two parameters which must be taken into account when evaluating performance. The first parameter is the number of range-resolution cells, which is dictated by the pulse bandwidth and the range depth of the object. Since GEO space objects have fewer range-resolution cells across them than a typical extended SAR scene, this parameter is an important contributor to PGA performance for ISAL imagery. The second parameter is the Carrier-to-Noise ratio (CNR). This parameter depends, in general, on the number of detected photons. For GEO space objects, ISAL systems operate in a photon-starved regime; thus, this parameter also contributes to PGA performance and should not be overlooked in the analysis.

This paper uses a high-fidelity wave-optics simulation tool known as *SimISAL* [3] to generate representative image data for input to a generic PGA algorithm. Throughout the analysis, emphasis is placed on finding the lower limits of performance for which image reconstruction is possible. In

1

so doing, this research characterizes the performance limitations of PGA for ISAL imagery as a function of CNR and the number of range-resolution cells across the scene. Section 2 of this paper reviews the necessary background information, Section 3 provides a description of the experimental parameter space, Section 4 discusses the results, and Section 5 provides a summary of the results with a brief description of future work.

2. BACKGROUND

Numerous autofocus algorithms exist in the literature to mitigate the effects of piston-phase errors in SAR imagery. One robust autofocus algorithm is PGA. Originally introduced in the late 1980's from the SAR research being performed at Sandia National Laboratories [4-7], PGA shares many similarities to the optical image processing algorithms of Labeyrie [8], Knox Thompson [9], and shift and add [10]. It also serves as a standard in most autofocus trade studies since PGA was thoroughly characterized by the mid 1990's [1, 11, 12]. Since then, much effort has gone into optimizing PGA's performance for SAR imagery [13-24].

To date, little has been published on PGA's performance for ISAL imagery. Gatt *et al.* performed a study which looked at the variance of the phase-difference estimator between pulses as a function of CNR [25]. This study was successful in characterizing PGA's performance at high CNRs. The results showed that for a uniformly illuminated diffuse rectangle object, the phase-difference estimator meets the Cramér-Rao bound (CRB) up to a saturation point. At high CNRs, speckle decorrelation dominates, and the results showed that the estimator variance does not meet the CRB. With this in mind, the following sub sections provide background information which help in characterizing the performance limitations of PGA for ISAL imagery at low CNRs.

Piston-Phase Error and Atmospheric Turbulence

When propagating light through a turbulent atmosphere, phase changes occur due to a non-uniform refractive index profile. These atmosphere-induced phase aberrations can efficiently be described by an orthogonal basis set such as Zernike polynomials. Piston, the first Zernike polynomial, is the average of the wavefront phase integrated across a circular aperture.

Typical non-coherent imaging systems are blind to piston aberrations since the average phase is not measured and does not affect image quality. In contrast, ISAL systems use heterodyne techniques to measure the phase of an optical signal averaged across the aperture. The return signal from a transmitted laser pulse is mixed with a reference pulse to estimate changes in phase over time. As such, atmospheric piston variations result in phase noise which corrupts the desired signal. While aperture-target motion, laser phase drift, and even sensor noise can contribute to unwanted phase variations in the ISAL data, these factors may be overcome by design before they corrupt the measured data.

Atmospheric piston variations, on the other hand, tend to dominate the raw data and can only be overcome by post processing.

In a well-designed system, the pulse duration is much shorter than the time scale of the atmospheric variations. All samples along the length of the pulse (the range dimension) encounter the same atmospheric piston change. However, as more and more pulses are concatenated to from a two-dimensional array, the changes in atmospheric piston create a phase variation in the cross-range dimension. This one-dimensional wavefront error acts to blur the reconstructed image along that dimension.

Post processing algorithms known as autofocus blindly estimate the one-dimensional wavefront error and deconvolve it from the image, thereby removing the blur. These algorithms take advantage of the fact that each sample in the return pulse (which translates to range bins when range compressed) experiences the same atmospheric piston effects. They assume that the object phase has zero mean and is statistically independent from range bin to range bin. Therefore, only atmospheric piston-phase errors are common across all range bins. Taking the ensemble average of either the phase or phase differences, improves estimation of the wavefront error. In low CNR conditions, the phase-error estimate for each range bin has a high variance, and more samples are needed for the ensemble average to converge to the true solution.

Generic Phase-Gradient Auto Focus Algorithm

PGA in its most generic form contains seven algorithmic steps [1, 11]. These steps are displayed in Figure 1 with a flow chart and image examples. Step 1 is to acquire complex image domain data which is blurred by piston-phase error. This data is then input into an iterative correction process. Step 2 is to shift the data. Here, the brightest scatterer in each range line is shifted to a user defined location (as shown, the left-most column of the data set) with wrap around from the edges. Step 3 incoherently sums along the shifted range lines to obtain a one-dimensional range average. An initial window is then determined by finding the 10 dB point from the peak and increasing the width by 50%. Subsequent windows decrease in width by 20% for each iteration [11].

Step 4 is to take the discrete Fourier transform (DFT) along the cross-range dimension to obtain range-compressed image domain data, $F(m, n)$, where m refers to the mth range line and n is the nth cross-range column. The phase differences $\Delta\hat{\phi}(n)$ are then estimated in Step 5 by using the following kernel:

$$\Delta\hat{\phi}(n) = arg\{\textstyle\sum_{m=1}^{M} F(m, n)F^*(m, n-1)\}. \qquad (1)$$

From Eq. (1), the entire aperture phase error $\hat{\phi}(n)$ is estimated by integrating the estimated phase differences $\Delta\hat{\phi}(n)$, viz.

$$\hat{\phi}(n) = \sum_{k=2}^{n} \Delta\hat{\phi}(k) \, ; \ \hat{\phi}(1) = 0. \qquad (2)$$

Step 5 continues by computing the root mean square (RMS) phase error and checks to see if it meets a threshold value of <0.5 rad. If yes, the algorithm is done; otherwise, the algorithm continues.
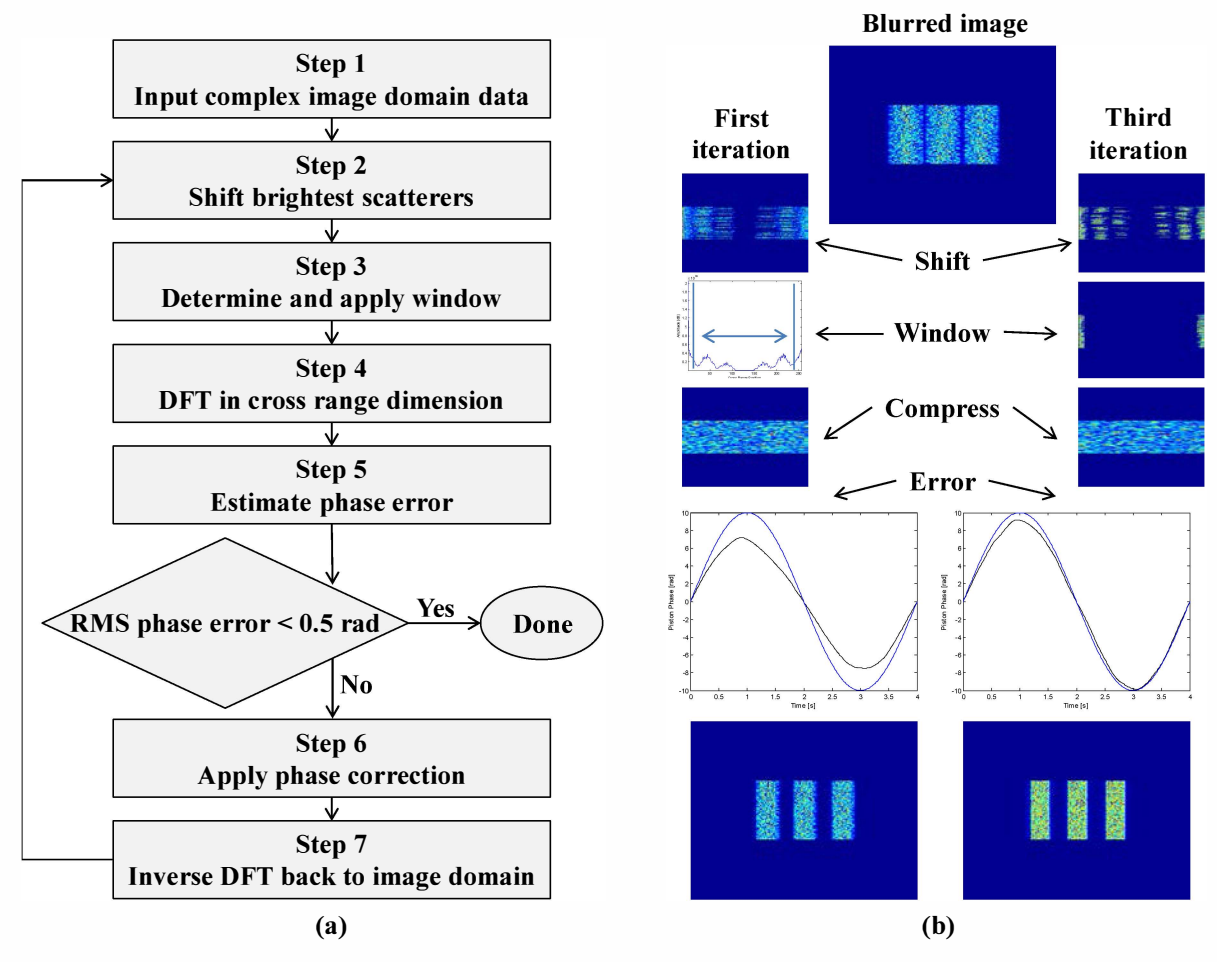

(a)

(b)

Figure 1 – A generic implementation of phase gradient autofocus (PGA). (a) describes the implemented algorithm with a flowchart, whereas (b) provides corresponding image examples.

Step 6 applies the phase correction. Mathematically, this manifests from Eq. (2), so that

$$F_c(m,n) = F(m,n)exp\big[-j\hat{\phi}(n)\big], \qquad (3)$$

where $F_c(m,n)$ is the corrected range-compressed image domain data. Step 7 takes the inverse DFT of the corrected range-compressed image domain data to acquire complex image domain data once again. The process is then repeated until the RMS phase error threshold value of <0.5 rad is achieved. In practice, this usually takes less than five iterations [1, 11]. Our implementation was limited to a maximum 100 iterations.

Comparison to the Cramér-Rao Bound

Previous assessments of autofocus performance [1, 25] have compared the observed empirical performance of autofocus algorithms to the CRB, which is a lower bound on the variance of an unbiased estimator. The idea is that if an algorithm can be shown to provide unbiased estimates and to

have variance matching the CRB, then it is optimal in the sense that no other unbiased estimator can have lower variance. However, the utility of these comparisons is limited in the sense that the CRB is target-dependent and the cited results address the CRB for a target consisting of a single point reflector per range line. This is representative of SAR imagery, but at optical wavelengths the targets are not strongly specular. In this work, we study performance trends as a function of CNR and number of range bins, but do not report target-specific CRB comparisons.

3. EXPERIMENTAL PARAMETER SPACE

In the following analysis, a high-fidelity wave-optics simulation tool known as *SimISAL* was used to generate representative ISAL imagery [3]. *SimISAL* uses a modular architecture, so that the wave-optics simulation, detector simulation, and image processing can be done independently of one another. As a result, parameters can be varied in each

3

module without having to rerun the entire simulation. This is an important step in the analysis due to the high computational requirements involved. *SimISAL* was developed exclusively in MATLAB® and uses AOTools [26] and WaveProp [27]. These robust MATLAB® toolboxes were created by the Optical Sciences Company (tOSC) specifically for simulations involving wave optics.

SimISAL is executed using the DoD High Performance Computing Modernization Program's (HPCMP) Enterprise Portal. The HPCMP Portal streamlines the use of HPC resources. MATLAB® code is dragged and dropped to a web browser of choice, where it is uploaded to the Portal and automatically distributed amongst the HPC nodes. While *SimISAL* was not developed to maximize parallelization, the Portal does allow multiple realizations or trades to be run simultaneously. With simulated seconds of run time requiring more than 40 hours of computational time, the Portal is a vital resource.

A simple three-bar object model (shown in Fig. 2) was used to generate images. The target had a single vertical rotation axis with no articulation. Some of the input parameters used are listed in Table 1. With this in mind, a single wave-optics simulation was used for all trades studies considered in this research. The number of range bins and CNR were varied in the detector and image processing modules. This allowed identical atmospheric and target effects to be applied for all test cases, as well as reducing the computational resources required.

Table 1 - Input parameters used to generate images.

Parameter	Value
Laser wavelength	1064 nm
Laser power	2 kW (scaled from 0.004-2)
Pulse repetition frequency	200 Hz
Duty cycle	100%
Wave-optics sample rate	400 Hz
Simulation time	8 s
Aperture diameter	4 m
Object rotation rate	1 μrad/s
Object OCS	$10\ m^2/sr$
Object zenith angle	45 degrees
Detector sample rate	100 kHz
Number of detectors	2
Quantum efficiency	0.5
A/D bits	8

Carrier-to-Noise Ratio

There are several different metrics used in practice to quantify a signal-to-noise ratio (SNR) for coherent imaging systems [29-31]. In this research, we use CNR which is defined as the ratio of the signal power P_s to the noise power P_n. It is equivalently defined in terms the number of detected signal photons N_s, so that

$$\text{CNR} = \frac{P_s}{P_n} = \eta_d\,\eta_h N_s, \qquad (4)$$

where η_d is the detector quantum efficiency and η_h is the heterodyne mixing efficiency. In well-designed ISAL systems, the dominate noise source is shot noise from the local oscillator. Shot noise acts like a noise floor which is present in all parts of the image. Depending on the strength of the target signal, the shot noise can swamp an image making it difficult to identify the object from the background. CNR is a legacy metric from the RF community. Loosely speaking, it is a SNR for shot noise limited detection processes. When using CNR, the variations due to speckle are ignored. As such, CNR is not limited to a value of one like the speckle SNR is [32]. This makes CNR a more useful metric when quantifying ISAL system performance.

Single-pulse, or range-compressed CNR refers to the value computed in the range-compressed domain. For ISAL systems, the image CNR is typically higher than range-compressed CNR since the image fill factor (ratio of object width to field-of-view) is less than one. In these cases, the range compressed signal density increases when cross-range compressed because the signal bandwidth is only a fraction of the total image bandwidth. This increase in signal density, relative to the noise floor, boosts the final image CNR proportionally. Since autofocus algorithms typically estimate phase errors in the range-compressed domain,
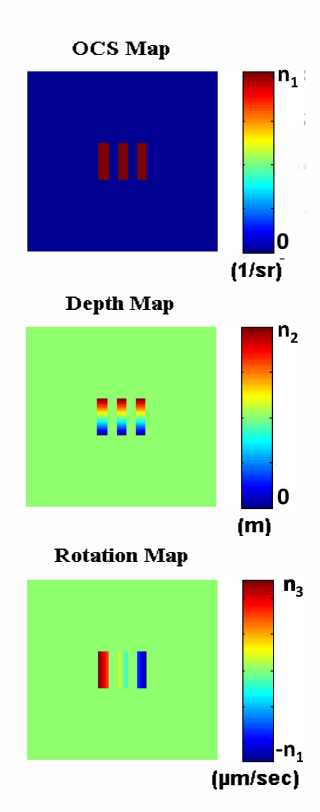

Figure 2 – The three-dimensional object model input into *SimISAL*. These three data maps provide optical cross section (OCS) reflectivity, depth/range, and rotation of each point in the x-y object plane.

performance will be shown as a function of range-compressed CNR in the analysis to follow.

For the trade studies conducted in this research, the CNR was varied by scaling the wave-optics return signal power by the laser power values given in Table 1. This was done prior to processing in the detector module of *SimISAL*. As a result, the detection efficiency remained fixed. Care was taken to adjust the power scaling to maintain the desired CNR as the number of range bins was changed. For each simulation, the theoretical CNR was computed based on the known signal strength and was also measured in the reconstructed images. Measuring the CNR of an image is straight forward for a uniform target, such as the three-bar target used in this research. In so doing, the mean power is measured over both the target and the background. The background power is then subtracted from the target power to get signal power, and the ratio of the signal power to the noise power is then calculated to obtain the measured CNR. Throughout the analysis, the measured CNR matched the theoretical estimate to within 10% error.

Range-Resolution Cells

Each range bin across the target allows an independent estimate of the cross-range phase error. As the number of range bins increases, the variance of the estimator decreases. This improves the correction process for autofocus algorithms. Therefore, both the CNR and the number of range bins should be considered when characterizing PGA's performance for ISAL imagery.

The idea of range bins may be foreign to most people even if they have image processing backgrounds. To make this concept manifest, consider Fig. 3. After mixing with the local oscillator, the return signal from a single pulse is composed of a D.C. term plus a superposition of crossterms with frequencies which depend on the range at which they were reflected, as shown in Fig. 3a. The spread of frequencies or object bandwidth ΔB_w, is determined by the linear-frequency-modulated (LFM) chirp rate β and the range depth z of the target. The total signal shown in Fig. 3b has a duration Δt, with sample period δt. This total signal can be thought of as a sum of Cosines multiplied by a rectangle function. When the signal is Fourier transformed, the result is delta functions, scaled by the object reflectivity at each observed frequency, which are convolved with a sinc function due to the finite duration Δt. For a tilted target with uniform reflectivity, each crossterm has equal amplitude and the result is similar to a rectangle function, as shown in Fig. 3c. Since frequency can be converted to range, the Fourier transform generates a one-dimensional image.
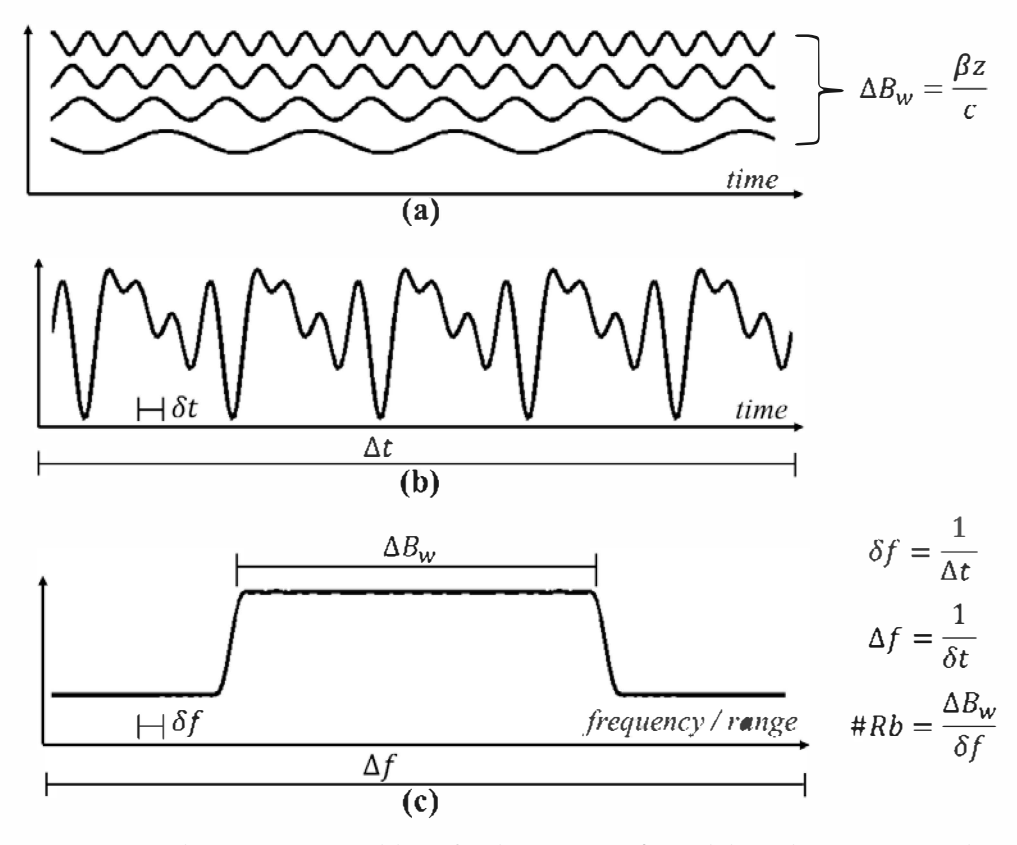

Figure 3 - Simple example showing the decomposition of a single pulse after mixing with the local oscillator (a), the superposition of all the beat frequencies (b), and the range compressed image (c). All variables are defined above in the main text.

5

There are three important quantities to consider in the range-compressed image. First, the total field of view or grid length is determined by the sample period δt in the time domain. Second, the sample rate should be high enough to sufficiently resolve the bandwidth ΔB_w of the object return, otherwise aliasing will occur. Finally, the frequency resolution δf or grid size in the image domain is determined by the total length of the pulse Δt. With this in mind, the number of range resolution cells $\#Rb$ comes from the ratio of ΔB_w to δf, and is effectively the number of resolution elements across the target's range extent. This number can be changed by either increasing the chirp rate β, and therefore the object bandwidth ΔB_w, or by increasing the pulse duration Δt, and therefore the frequency resolution δf. For this study, the chirp rate was scaled to obtain the desired number of range bins. This allowed the pulse duration and number of pulses to remain constant for all cases studied.

4. RESULTS AND DISCUSSION

Two types of piston phase errors were considered in this research, realistic variations simulated using *SimISAL* which have been validated against Kolmogorov theory, and the extreme case of white phase noise with random draws for each pulse uniformly distributed in the range (-π, π]. The RMS phase difference between the simulated piston and the PGA solution was used as a metric to measure performance. While several other metrics were considered including Strehl ratio and image/phase correlations, the RMS phase difference was found to be the most robust in characterizing where PGA fails at low CNR values—the overall goal of this research.

Atmospheric Piston-Phase Error

Figure 4 shows the simulated piston from *SimISAL* over a two second period. The black line is the simulated piston, and the blue line is the solution that PGA uses to correct the blurred image for this particular case. The cyan line is the difference between the two and is used to compute the RMS value. This piston phase was used for all cases considered (except for the white noise cases which will be discussed below).

Figure 5 shows the RMS phase difference as a function of CNR and the number of range bins. It is the ensemble average of 10 separate realizations each having independent shot noise. Initial testing showed that this parameter space adequately captured the points at which PGA failed. This can be clearly seen by the difference between the dark blue region in the top right where PGA reduced the RMS down to a few radians, and the multicolor region in the lower left, where PGA failed resulting in very large RMS values. Figure 6 shows slice plots of Fig. 5 for each of the 10 separate range bin values. The sharp drop in RMS as a function of CNR shows that PGA either corrects an image

well down to approximately 1 rad RMS, or it fails and creates huge phase errors of greater than 100 rad RMS. There is very little transition between the two extremes. Figure 6 also shows how this point of failure moves to lower CNR values as the number of range bins increases. With 50 range bins PGA works down to CNRs of approximately 0.3. Many ISAL applications may not have this many range bins, and must compensate by improving the CNR in order to correct slow-time piston phase errors.
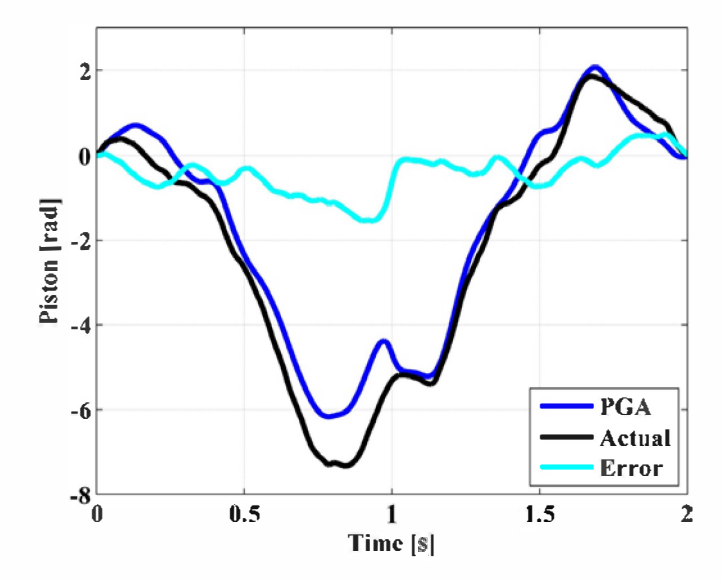

Figure 4 – The simulated atmospheric piston-phase error from *SimISAL* (color available online).
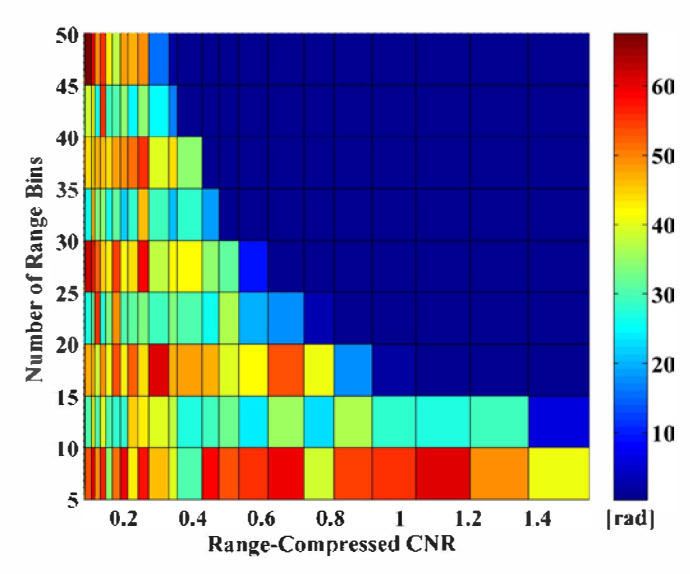

Figure 5 - RMS phase error as a function of the number of range bins and range-compressed CNR for the simulated atmospheric piston-phase error. The number of range bins is varied over ten values ranging from 5-50 range bins, and the CNR is varied over 24 values ranging from 0.2 to 2.
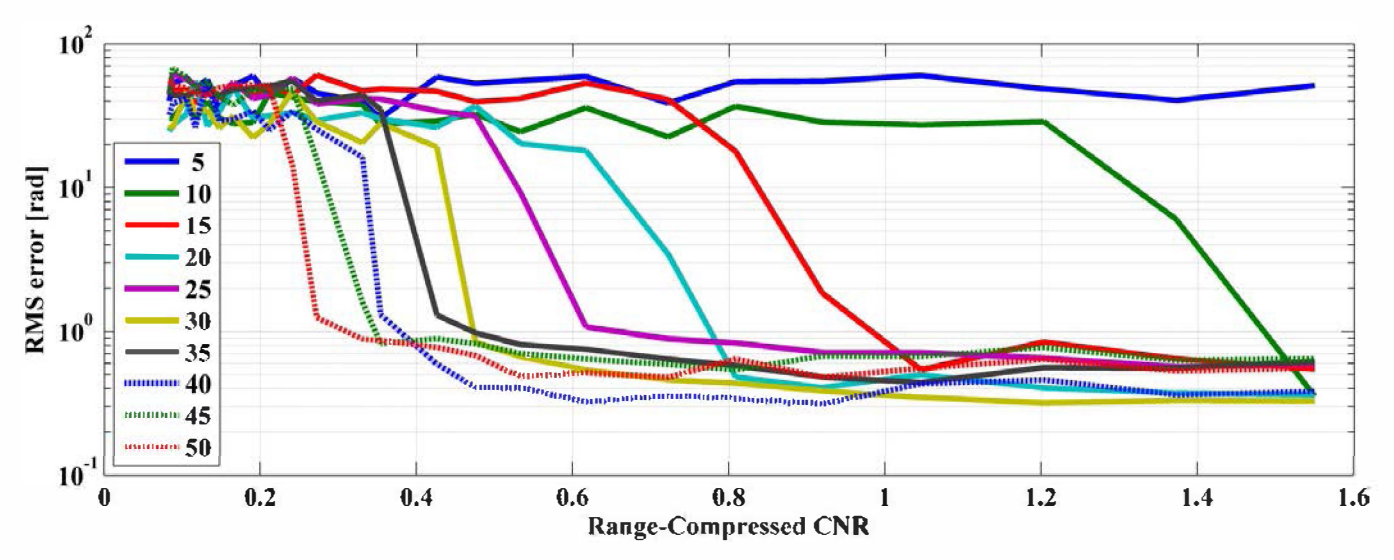
Figure 6 – Slice plots of Fig. 5 showing RMS error versus range-compressed CNR for the simulated atmospheric piston-phase error (color available online).
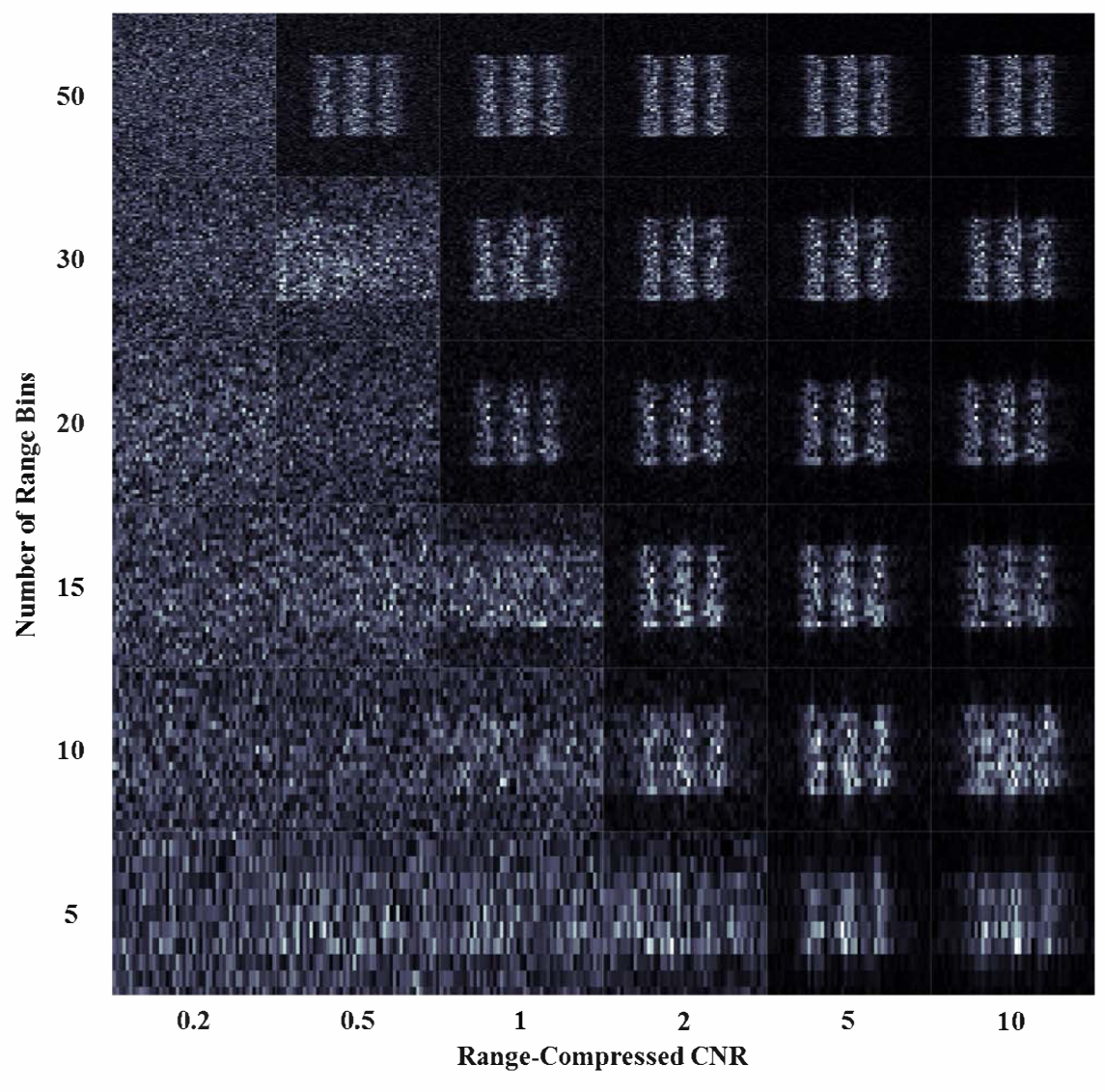

Figure 7 – Reconstructed images with the same realization seed of shot noise for the simulated atmospheric piston-phase error. The images are concatenated together as a function of the number of range bins and range-compressed CNR.

The same results that were presented above for realistic atmospheric piston-phase errors are also presented below for white-phase noise in Figs. 8-11. Figure 8 shows the extremely high variance of the white-phase noise after it has been unwrapped. While PGA follows it closely, the large variations lead to higher RMS values obtained from the cyan line. Even though the RMS values are higher, the PGA solution is still able to sharpen the reconstructed image. This behavior is consistent with the results of Wahl *et al.* [11]. Figures 9-11 show similar performance as seen above; however, the failure points have been shifted to higher CNRs. This means that PGA requires higher CNR to reconstruct an image when the phase is rapidly changing from pulse to pulse. In addition, the "knee in the curve" is less distinguished in terms of where PGA fails. It is conjectured that this "blurring" of the performance limitations is a result of the higher phase differences obtained from the representative data given in Fig. 8. This point is a topic of future research.

5. CONCLUSION

This paper extends previous efforts in PGA performance analysis by using high-fidelity wave-optics simulation and realistic atmospheric piston variations to characterize how well the algorithm works on ISAL imagery in low CNR environments. White piston phase noise was also considered to help find performance limitations under worse-case conditions. A representative ISAL target was used and the number of range bins was varied along with CNR. The RMS phase error of the PGA correction was then computed. This allowed the performance limitations of PGA to be fully mapped out over a wide parameter space.

The results showed cutoffs in PGA performance as a function of the number of range bins and the CNR. PGA either improved the image or made it worse by adding significant phase errors. As the number of range bins increased, PGA required less CNR to perform. While this is not a new concept, we can now use this mapping to design ISAL systems which use PGA to correct slow-time phase errors. While many SAR or SAL images may have a large number of range bins, ISAL targets may not offer the same benefit. Therefore, precisely understanding how much CNR is needed given a smaller number of range bins is extremely important to ISAL system design.

Future work will focus on testing several of the PGA optimizations that have been published. Characterizing performance of two-dimensional autofocus algorithms is also of interest. These are necessary when the piston is not constant during a single pulse. Such is the case for longer pulses or higher frequency phase errors.
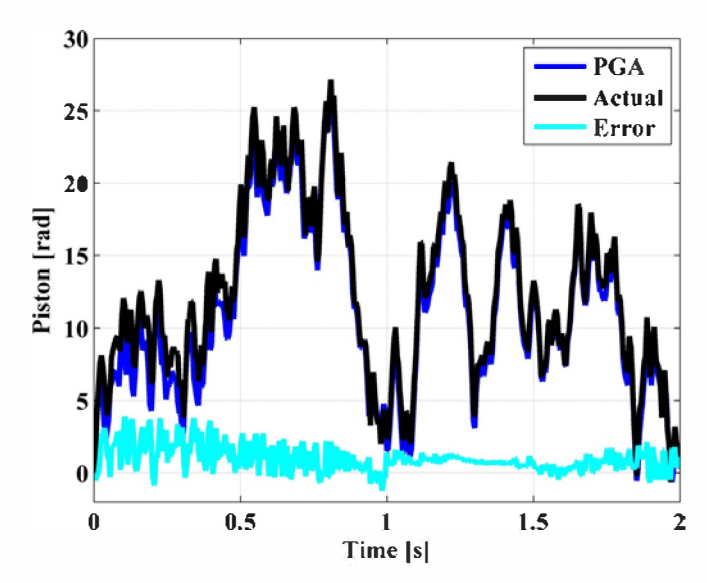

Figure 8 – The simulated white noise piston-phase error (color available online).
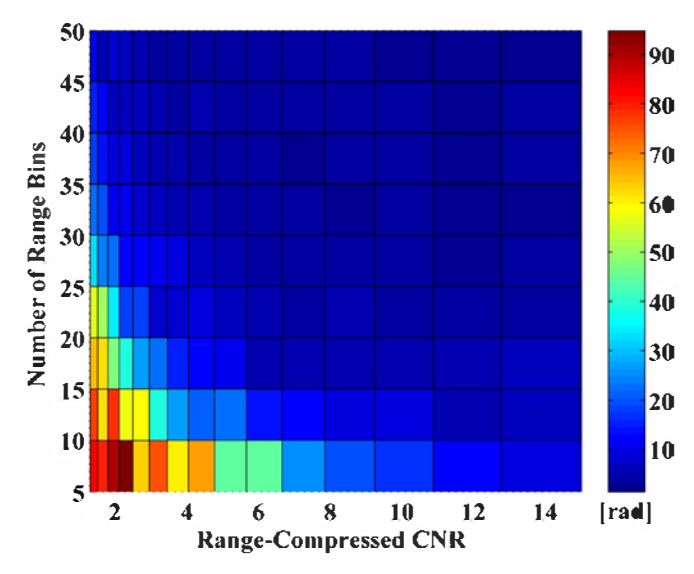

Figure 9 - RMS phase error as a function of the number of range bins and range-compressed CNR for the simulated white noise piston-phase error. The number of range bins is varied over ten values ranging from 5-50 range bins, and the CNR is varied over 24 values ranging from 2 to 100.
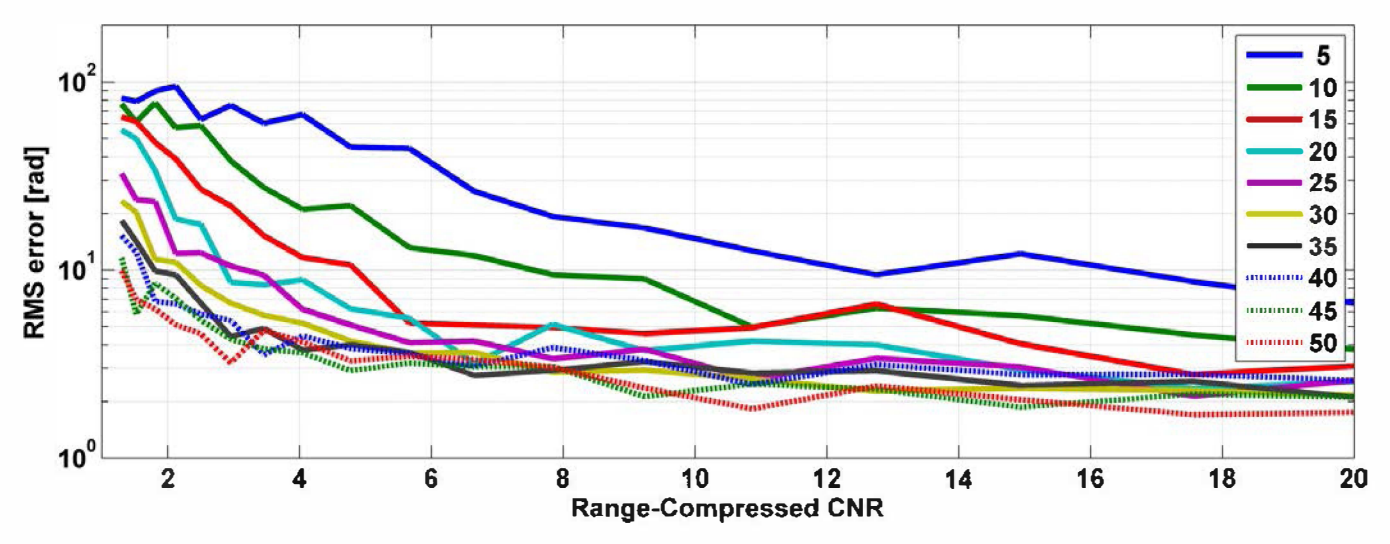
Figure 10 – Slice plots of Fig. 9 showing RMS error versus range-compressed CNR for the simulated white noise piston-phase error (color available online).
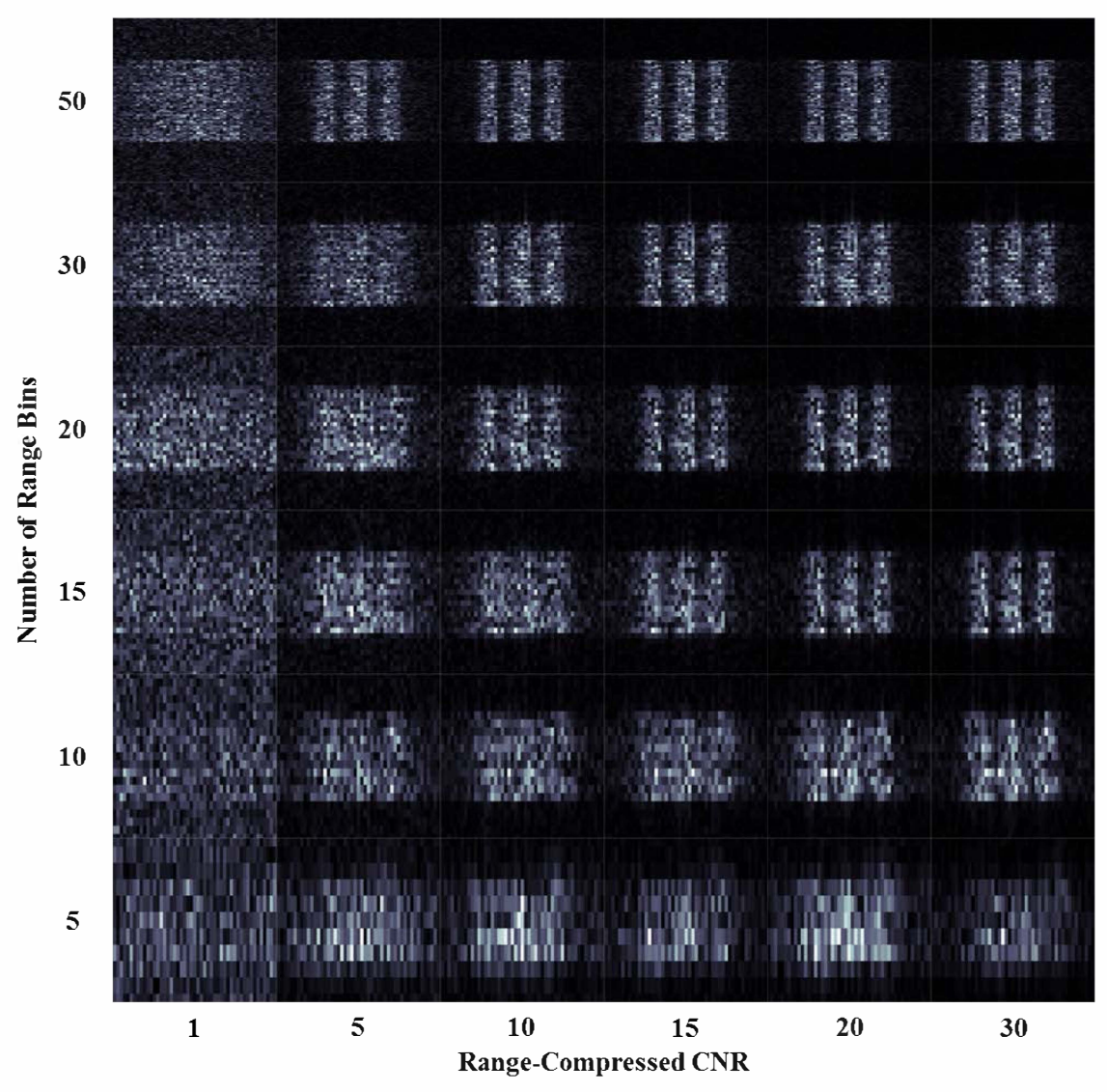

Figure 11 – Reconstructed images with the same realization seed of shot noise for the simulated white noise piston-phase error. The images are concatenated together as a function of the number of range bins and range-compressed CNR.

REFERENCES

1. C. V. Jakowatz, Jr., D. E. Wahl, P. H. Eichel, D. C. Ghiglia, and P. A. Thompson, [Spotlight-Mode Synthetic Aperture RADAR: A Signal Processing Approach], Springer (1996).

2. C. J. Pellizzari, C. L. Matson, V. S. Gudimetla, "Inverse synthetic aperture LADAR for geosynchronous space objects—signal to noise analysis," Proc. AMOS Conference (2011).

3. C. J. Pellizzari, M. F. Spencer, N. K. Steinhoff, J. Belsher, G. A. Tyler, S. Williams, S. E. Williams, "Inverse synthetic aperture LADAR: A high-fidelity modeling and simulation tool," Proc. SPIE **8877** (2013).

4. P. H. Eichel, D. C. Ghiglia, and C. V. Jakowatz, Jr., "Speckle processing method for synthetic-aperture-radar phase correction," Opt. Lett. **14**, 1 (1989).

5. P. H. Eichel and C. V. Jakowatz, Jr., "Phase-gradient algorithm as an optimal estimator of the phase derivative," Opt. Lett. **14**, 1101 (1989).

6. D. C. Ghiglia and G. A. Mastin, "Two-dimensional phase correction of synthetic-aperture-radar imagery," Opt. Lett. **14** 1104 (1989).

7. United States Patent No. 4,924,229, P. H. Eichel, D. C. Ghiglia, and C. V. Jakowatz, Jr., "Phase Correction System for Automatic Focusing of Synthetic Aperture Radar," May 8 (1989).

8. A. Labeyrie, "Attainment of Diffraction Limited Resolution in Large Telescopes by Fourier Analysing Speckle Patterns in Star Images," Astron. & Astrophys. **6**, 85 (1970).

9. K. T. Knox and B. J. Thompson, "Recovery of Images from Atmospherically Degraded Short-Exposure Photographs," Astrophys. J. **193**, L45 (1974).

10. R. H. T. Bates and F. M. Cady, "Towards True Imaging by Wideband Speckle Interferometry," Opt. Commun. **32**, 365 (1980).

11. D. E. Wahl, P. H. Eichel, D. C. Ghiglia, and C. V. Jakowatz, Jr., "Phase Gradient Autofocus—A Robust Tool for High Resolution SAR Phase Correction," IEEE Trans Aerospace & Elec. Systems **30**, 827 (1994).

12. W. G. Carrara, R. S. Goodman, and R. M. Majewski, [Spotlight Synthetic Aperture Radar Signal Processing Algorithims], Artech House (1995).

13. C. V. Jakowatz Jr. and D. E. Wahl, "Eigenvector method for maximum-liklihood estimation of phase errors in synthetic-aperture-radar imagery," J. Opt. Soc. Am A **10**, 2539 (1993).

14. F. Berizzi and G. Corsini, "Autofocusing of Inverse Synthetic Aperture Radar Images Using Contrast Optimization," IEEE Trans Aerospace & Elec. Systems **30**, 1185 (1996).

15. H. L. Chan and T. S. Yeo, "Noniterative Quality Phase-Gradient Autofocus (QPGA) Algorithm for Spotlight SAR Imagery," IEEE Trans. Geosci. Remote Sensing **36**, 1531 (1998).

16. W. Ye, T. S. Yeo, and Z. Bao, "Weighted Least-Squares Estimation of Phase Errors for SAR/ISAR Autofocus," IEEE Trans. Geosci. Remote Sensing **37**, 2487 (1999).

17. J. R. Fienup, "Synthetic-aperture radar autofocus by maximizing sharpness," Opt. Lett. **25**, 221 (2000).

18. W. L. Van Rossum, M. P. G. Otten, and R. J. P. Van Bree, "Extended PGA for Range Migration Algorithms," IEEE Trans Aerospace & Elec. Systems **42**, 478 (2006).

19. Z. She and Y. Liu, "Autofocus for ISAR Imaging Using Higher Order Statistics," IEEE Trans. Geosci. Remote Sensing **5**, 299 (2008).

20. R. J. C. Middleton, D. G. Macfarlane, and D. A. Robertson, "Range autofocus for linearly frequency-modulated continuous wave radar," IET Radar Sonar Navig. **5**, 288 (2011).

21. Y. Li, C. Liu, Y. Wang, and Q. Wang, "A Robust Motion Error Estimation Method Based on Raw Data," IEEE Trans. Geosci. Remote Sensing **50**, 2780 (2012).

22. L. Zhang, Z. Qiao, M. Xing, L. Yang, and Z. Bao, "A Robust Motion Compensation Approach for UAV SAR Imargery," IEEE Trans. Geosci. Remote Sensing **50**, 3202 (2012).

23. D. Zhu, R. Jiang, X. Mao, and Z. Zhu, "Multi-Subaperture PGA for SAR Autofocusing," IEEE Trans Aerospace & Elec. Systems **49**, 468 (2013).

24. K. H. Liu, A. Wiesel, and D. C. Munson, Jr., "Synthetic Aperture Radar Autofocus via Semidefinite Relaxation," IEEE Trans. Image Process. **22**, 2317 (2013).

25. P. Gatt, D. Jacob, B. Bradford, J. Marron, and B. Krause, "Performance bounds of the phase gradient autofocus algorithm for synthetic aperture ladar," Proc. SPIE **7323** (2009).

26. T. J. Brennan, and P. H. Roberts, "AOTools The Adaptive Optics Toolbox for Use with MATLAB Version 1.4," User manual, the Optical Sciences Company, Anaheim CA (2010).

27. T. J. Brennan, P. H. Roberts, and D. C. Mann, "WaveProp A Wave Optics Simulation System for Use with MATLAB," User manual, the Optical Sciences Company, Anaheim CA (2010).

28. Maui High Performance Computing Center "DoD HPCMP MHPCC DSRC Enterprise Portal," <http://www.mhpcc.hpc.mil/portal/index.html> (16 Oct 2013).

29. T. J. Karr, "Signal-to-Noise Ratio of Coherent Imaging LADAR," Proc. of SPIE **6712** (2007).

30. R. L. Lucke and L. J. Rickard, "Photon-limited synthetic-aperture imaging for planet surface studies," Applied Optics, Vol. 41, No. 24, (2002)

10

31. D. G. Youmans, "Round-trip turbulence ladar scintillation modeling using data fits and resulting signal-to-noise ratio," Proc. of SPIE **5413** (2004)

32. J. W. Goodman, [Speckle Phenomena in Optics, Theory and Applications], Roberts and Company (2007).

BIOGRAPHIES

Casey J. Pellizzari received a BSEE from California State University, Fullerton in 2005, and his MSEE in Electro-Optics at the Air Force Institute of Technology (AFIT) in 2010. He currently serves as Deep Space Imaging Lead for the Directed Energy Directorate, Air Force Research Laboratory, Kihei, HI. Capt Pellizzari's research interests include strong turbulence adaptive optics (AO), 24 hour non-AO image enhancement, and non-traditional imaging techniques.

Mark F. Spencer is a PhD candidate in Optical Sciences and Engineering at the Air Force Institute of Technology (AFIT) within the Department of Engineering Physics. Upon completion of his doctoral studies under a SMART Scholarship, he will pursue a career with the Air Force Research Laboratory's Directed Energy Directorate. Mark graduated from the University of Redlands in 2008 with a BS in Physics and from AFIT in 2011 with a MS in Optical Sciences and Engineering.

Brandoch Calef is an imaging scientist with Boeing. For ten years, he has supported the AFRL space surveillance site on Maui. His research interests include image reconstruction, atmospheric statistics, estimation theory, optical instrumentation, and high-performance computing. He received a PhD in Applied Mathematics from the University of California Berkeley.

Jeremy Bos is currently serving as postdoctoral fellow at the Air Force Research Laboratory investigating deep turbulence effects on laser propagation and imaging under the National Research Council's Research Associateship Program. Before beginning this appointment Dr. Bos completed his Ph.D. in Electrical Engineering in August 2012 from Michigan Technological University. Before returning to pursue his Ph.D., Dr. Bos spent 10 years in the automotive and defense industries.

Skip Williams received joint BS degrees in Chemistry and Physics from the University of Arkansas in 1988 and a Ph.D. in Chemical Physics from Stanford University in 1994. Part of his Ph.D. thesis work was completed at the Sandia National Laboratories, and he started his research career with a Postdoctoral appointment at Los Alamos National Laboratory from 1994-1996. Since 1996, he has conducted research at the Air Force Research Laboratory and is currently the Chief Engineer at the Air Force Maui Optical and Supercomputing (AMOS) site. His current research focusses on inverse synthetic aperture LADAR for imaging space assets beyond the normal resolvable range of optics based on aperture diameter encompassing electro-optics, laser propagation, adaptive optics, and signal processing activities.

Daniel C. Senft has over 25 years of experience in laser remote sensing. He received his Ph.D. from the University of Illinois in 1991, where he developed, operated, and analyzed results from lidars for the study of the upper atmosphere. His field experiment experience includes measurements at the Amundsen-Scott South Pole Station, Australia, Spitzbergen Island (Norwegian Arctic), and Hawaii (Mauna Kea Observatory). He has worked for the Air Force Research Laboratory since 1993 on development, field experiments, and flight testing of laser systems for chemical detection, satellite vibrometry, active characterization, laser communication, and laser imaging.

Stacie E. Williams serves as a lead technical investigator and Subject Matter Expert for the AFRL Directed Energy Directorate at the Air Force Maui Optical and Supercomputing Site (AMOS) and has published over 25 journal articles in peer reviewed professional publications. Dr. Williams works on several optical and laser programs that include improving our daylight imaging capabilities and developing deep space imaging for space situational awareness. Dr. Williams directs community outreach efforts consisting of STEM teacher education, curriculum development, and internship and mentor programs. She received her Ph.D. from the University of California at Santa Cruz.

11